An Efficient, Full-Potential Implicit Method Based on Characteristics for Supersonic Flows

Vijaya Shankar*
Rockwell International Science Center, Thousand Oaks, California
and
Stanley Osher†
University of California, Los Angeles, California

A nonlinear aerodynamic prediction technique based on the full-potential equation in conservation form has been developed for the treatment of supersonic flows. The method uses the theory of characteristic signal propagation to accurately simulate the flow structure, which includes shock waves and mixed elliptic-hyperbolic crossflow. An implicit approximate factorization scheme is employed to solve the finite-differenced equation. The necessary body-fitted grid system in every marching plane is generated numerically, using an elliptic grid solver. Results are shown for conical and nonconical wing-body combinations and compared with experimental data and Euler calculations. The method demonstrates an enormous savings in execution time and memory requirements over Euler methods.

I. Introduction

NONLINEAR aerodynamic prediction techniques based on the Euler equations[1-3] and the full-potential equation[4-7] are steadily maturing into complex aerodynamic tools and becoming an attractive alternate approach to using the linearized panel methods.[8] Panel methods can handle very complicated geometries requiring minimal computer time to provide less accurate results, while the Euler solvers need expensive computer runs even for simple wing-body configurations. The full-potential methods[6,7] are a substitute for the Euler methods[1,3] to avoid the requirement of excessive computer time and memory allocation. While using a full-potential method for supersonic flows, one should be aware of the isentropic limitations of the theory. As a general rule, the full-potential theory is expected to perform well when the product of the Mach number and the characteristic flow deflection angle is less than 1 ($M\delta \leq 1$).

The full-potential method of Refs. 4-6 is based on the nonconservative form of the equation, while Ref. 7 and the present paper deal with the conservative form, to conserve mass across the shock.[9,10] In order to properly treat the supersonic flow structure, which includes shock waves and mixed elliptic-hyperbolic crossflow, the present method uses the theory of characteristic signal propagation based on the eigenvalue system of the full-potential equation. An approximate factorization implicit scheme, which includes a density biasing procedure in the crossflow plane, is incorporated to accelerate the computational efficiency. The density biasing procedure is activated by the eigenvalue system and properly takes into account the direction of the crossflow. The implicit approximate factorization scheme does not pose any restrictions on the direction of sweep that are present in the successive line overrelaxation method (SLOR).[4-6]

The full-potential as well as Euler methods require the application of boundary conditions at the actual body surface location. This, in general, necessitates the use of a body-fitted coordinate system. In the present method, the equation is cast in a more general arbitrary coordinate system and the appropriate body-fitted grid is generated numerically, employing an elliptic grid solver.[11]

The paper presents various results for conical and nonconical wing-body configurations and comparison is made with experimental data and Euler solution. The effect of the density biasing based on the characteristic signal propagation is demonstrated in terms of a sharper pressure profile across the shock wave. References 5 and 6 present excellent results at low supersonic Mach numbers, while Ref. 7 and the present paper demonstrate the capability of the conservative full-potential approach in handling even very high Mach number flows ($M_\infty \sim 4$-6, $\alpha \sim 0$-8 deg). All of the calculations reported in this paper were performed using the CDC 7600 computer and clearly demonstrated an order-of-magnitude or more reduction in computer time over Euler methods. A typical nonconical wing-body calculation takes less than 2 min of execution time to produce results comparable with experimental data.

II. Formulation

The conservative full-potential equation cast in an arbitrary coordinate system defined by $\zeta=\zeta(x,y,z)$, $\eta=\eta(x,y,z)$, and $\xi=\xi(x,y,z)$ takes the form

$$\left(\rho\frac{U}{J}\right)_\zeta+\left(\rho\frac{V}{J}\right)_\eta+\left(\rho\frac{W}{J}\right)_\xi=0 \tag{1}$$

where U, V, and W are the contravariant velocity components. Introducing the following notation for convenience

$$U=U_1, \quad V=U_2, \quad W=U_3$$

$$x=x_1, \quad y=x_2, \quad z=x_3$$

$$\zeta=X_1, \quad \eta=X_2, \quad \xi=X_3$$

the contravariant velocities and density are given by

$$U_i=\sum_{j=1}^{3} a_{ij}\phi_{X_j} \qquad i=1,2,3$$

...

Presented as Paper 82-0974 at the AIAA/ASME Third Joint Thermophysics, Fluids, Plasma and Heat Transfer Conference, St. Louis, Mo., June 7-11, 1982; submitted July 7, 1982; revision received Dec. 23, 1982.

*Manager, CFD Group. Associate Fellow AIAA.
†Professor, Department of Mathematics.

$$a_{ij}=\sum_{k=1}^{3}\frac{\partial X_i}{\partial x_k}\frac{\partial X_j}{\partial x_k}\qquad \begin{matrix} i=1,2,3 \\ j=1,2,3 \end{matrix}$$

$$\rho=\left[1-\left(\frac{\gamma-1}{2}\right)M_\infty^2\{U\phi_\zeta+V\phi_\eta+W\phi_\xi-1\}\right]^{1/(\gamma-1)} \quad (2)$$

The Jacobian of the transformation J is represented by

$$J=\frac{\partial(\zeta,\eta,\xi)}{\partial(x,y,z)}=\begin{bmatrix}\zeta_x & \zeta_y & \zeta_z\\ \eta_x & \eta_y & \eta_z\\ \xi_x & \xi_y & \xi_z\end{bmatrix} \quad (3)$$

Equation (1) is in terms of a general coordinate system (ζ,η,ξ) and can accommodate any kind of mapping procedure, either analytical (conformal mapping) or numerical. Use of Eq. (1) to simulate the supersonic flow by marching in the ζ direction first requires the establishment that the equation is indeed hyperbolic with respect to the marching direction. The nature of Eq. (1) can be analyzed by studying its eigenvalue system. Combining the irrotationality condition in the (ζ,η) and (ζ,ξ) plane and Eq. (1), one can write the following matrix equation:

$$Aq_\zeta+Bq_\eta+Cq_\xi=0 \quad (4)$$

where

$$A=\begin{bmatrix}(1/J)(\rho U)_{\phi_\zeta} & (1/J)(\rho U)_{\phi_\eta} & (1/J)(\rho U)_{\phi_\xi}\\ 0 & 1 & 0\\ 0 & 0 & 1\end{bmatrix}$$

$$B=\begin{bmatrix}(1/J)(\rho V)_{\phi_\zeta} & (1/J)(\rho V)_{\phi_\eta} & (1/J)(\rho V)_{\phi_\xi}\\ -1 & 0 & 0\\ 0 & 0 & 0\end{bmatrix}$$

$$C=\begin{bmatrix}(1/J)(\rho W)_{\phi_\zeta} & (1/J)(\rho W)_{\phi_\eta} & (1/J)(\rho W)_{\phi_\xi}\\ 0 & 0 & 0\\ -1 & 0 & 0\end{bmatrix}$$

$$q=\begin{bmatrix}\phi_\zeta\\ \phi_\eta\\ \phi_\xi\end{bmatrix}$$

The subscripts in Eq. (4) denote differentiation with respect to that variable.

In order for Eq. (4) or Eq. (1) to be hyperbolic in the ζ direction, the following two conditions must be satisfied:

1) A^{-1} must exist.

2) All real linear combinations of $A^{-1}B$ and $A^{-1}C$ must have real eigenvalues (characteristics). This implies $A^{-1}(\alpha B+\beta C)$ must have real eigenvalues for all combinations of α and β satisfying $\alpha^2+\beta^2=1$.

When the two conditions are applied to Eq. (4), the following criterion is obtained for ζ to be the marching direction.

$$(\rho U)_{\phi_\zeta}=\rho\left(a_{11}-\frac{U^2}{a^2}\right)<0 \quad (5)$$

where the transformation metric a_{11} is defined in Eq. (2) and a is the local speed of sound. Equation (5) is the most general form. For example, in a spherical system (r,θ,ϕ), for the radial direction r to be the marching direction, according to Eq. (5), the radial velocity q_r must be supersonic. In a Cartesian system (x,y,z), for x to be the marching direction, the velocity u must be supersonic. For convenience, the derivation of Eq. (5) for a Cartesian system is described in Appendix A, and the derivation for an arbitrary coordinate system (ζ,η,ξ) has been derived in a similar manner.

Thus far, the condition for ζ to be a marching direction has been identified from the characteristic theory. This means the (η,ξ) plane will be treated as a marching plane, which will be defined from here on in this paper as the crossflow plane (the real crossflow is the projection of the velocity vector on a unit sphere with center at the origin). Even though the flow is supersonic in the marching direction (i.e., hyperbolic type), the behavior of the flow structure in the crossflow plane (η,ξ) can be a mixed elliptic-hyperbolic type. Depending on the nature of the flow at a crossflow plane grid point (whether elliptic, parabolic, or hyperbolic), the η and ξ derivative terms in Eq. (1) will be appropriately modeled. Again, the theory of characteristics will dictate how the signals are propagated in the crossflow plane.

A. Crossflow Signal Propagation

The nature of the flow in the (η,ξ) plane can be analyzed by separately studying the eigenvalues of $A^{-1}B$ and $A^{-1}C$. The eigenvalue character of $A^{-1}B$ will determine the η-derivative treatment and similarly $A^{-1}C$ for the ξ derivative. For illustration, only the study of $A^{-1}B$ is shown here, and $A^{-1}C$ follows the same procedure.

The eigenvalues λ of $A^{-1}B$ are obtained by setting the determinant $|A^{-1}B-\lambda I|=0$. Since A^{-1} is assumed to exist [condition 1 preceding Eq. (5)], the following is true.

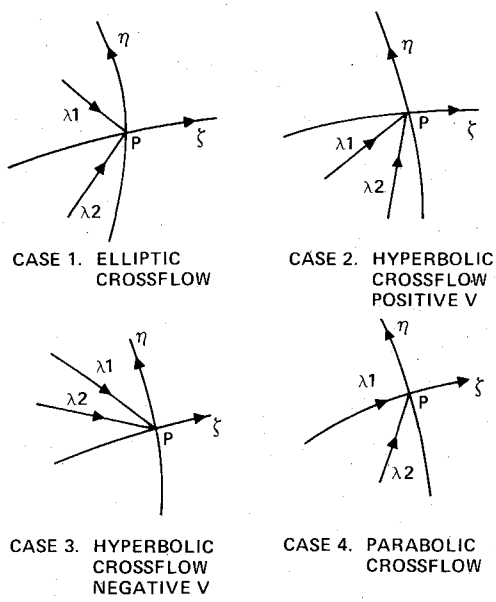

Fig. 1 Eigenvalue structure in (ζ,η) plane.

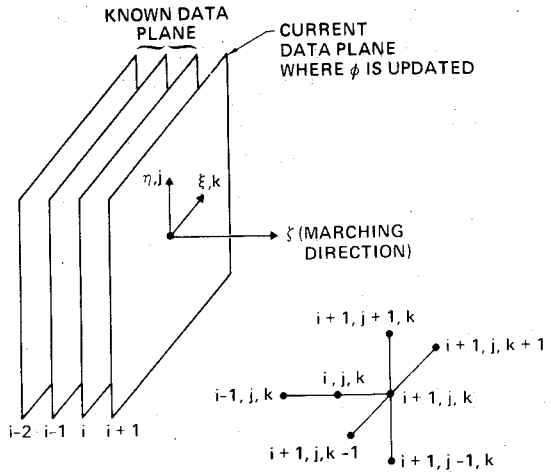

Fig. 2 Implicit computational molecule.

$$|B-\lambda A| = \begin{bmatrix} \frac{1}{J}(\rho V)_{\phi_\zeta} - \frac{\lambda}{J}(\rho U)_{\phi_\zeta} & \frac{1}{J}(\rho V)_{\phi_\eta} - \frac{\lambda}{J}(\rho U)_{\phi_\eta} & \frac{1}{J}(\rho V)_{\phi_\xi} - \frac{\lambda}{J}(\rho U)_{\phi_\xi} \\ -1 & -\lambda & 0 \\ 0 & 0 & -\lambda \end{bmatrix} = 0 \tag{6}$$

Solving for λ from Eq. (6), one gets

$$\lambda_{1,2} = \frac{\{(\rho U)_{\phi_\eta} + (\rho V)_{\phi_\zeta}\} \pm \sqrt{\{(\rho U)_{\phi_\eta} + (\rho V)_{\phi_\zeta}\}^2 - 4(\rho U)_{\phi_\zeta}(\rho V)_{\phi_\eta}}}{2(\rho U)_{\phi_\zeta}} \tag{7}$$

When Eq. (5) is satisfied, the discriminant in Eq. (7) is always positive.

Now, analyzing λ_1 and λ_2, the following combinations are possible.

1) λ_1 is positive and λ_2 is negative, or λ_1 is negative and λ_2 is positive.
2) λ_1 and λ_2 are both positive.
3) λ_1 and λ_2 are both negative.
4) λ_1 or λ_2 is zero.

These possible combinations are schematically shown in Fig. 1. Each one of these combinations describes a different feature of the flow in the crossflow direction η. Referring to the diagrams of Fig. 1, the following descriptions are made.

Case 1

Here, one eigenvalue is positive and one negative. This implies an *elliptic-type* crossflow because the characteristic signals are brought into point P from both the positive and negative direction of η.

Case 2

Here, both the characteristics are positive, which means the characteristic signals propagate into point P only from below and anything happening above point P does not influence that point. This describes a *hyperbolic-type* crossflow point with a positive contravariant velocity V.

Case 3

Here, the characteristic signals propagate from above into point P and, similar to case 2, this describes a *hyperbolic-type* crossflow with a negative contravariant velocity V.

Case 4

Here, one of the eigenvalues is zero and describes a *parabolic-type* crossflow. This will represent the crossflow sonic line.

The transition from an elliptic to a hyperbolic crossflow type takes place through a parabolic point, which is indicated by one of the eigenvalues going to zero. Thus, by monitoring the eigenvalues λ_1 and λ_2, one can precisely model the crossflow plane terms. Depending on whether it is elliptic or hyperbolic, appropriate finite-difference models for the η-derivative term in Eq. (1) are chosen. This will be described later in this paper.

One can readily see from Eq. (7) that one of the eigenvalues goes to zero when $(\rho V)_{\phi_\eta} = 0$. From the definition of ρ and V from Eq. (2), one can write

$$(\rho V)_{\phi_\eta} = \rho\left\{a_{22} - \frac{V^2}{a^2}\right\} \tag{8}$$

Thus, when $a_{22} = V^2/a^2$ occurs, the method will anticipate a switch in the character of the crossflow and realize the onset of the formation of a supercritical crossflow.

Besides providing valuable information regarding the type of crossflow, the eigenvalues λ_1 and λ_2 of $A^{-1}B$ and, similarly, λ_3 and λ_4 of $A^{-1}C$ can also be used to determine the marching step size $\Delta\zeta$ from a given Courant number.

$$\Delta\zeta = \min\left\{\frac{\mathrm{CFL}^*\Delta\eta}{(\lambda_{\max})_\eta}, \quad \frac{\mathrm{CFL}^*\Delta\xi}{(\lambda_{\max})_\xi}\right\} \tag{9}$$

The quantities $(\lambda_{\max})_\eta$ and $(\lambda_{\max})_\xi$ define the maximum of (λ_1,λ_2) and (λ_3,λ_4), respectively, and CFL is the user-prescribed Courant number, usually set to values much greater than one for implicit schemes (CFL ~ 5-20).

B. Treatment of $(\rho U/J)_\zeta$ in Eq. (1)

The direction ζ has been identified to be the hyperbolic marching direction satisfying the condition given by Eq. (5). Referring to Fig. 2, this derivative term will be backward differenced as

$$\left(\rho\frac{U}{J}\right)_\zeta = \frac{(a_1-\theta b_1)\left\{\left(\rho\frac{U}{J}\right)_{i+1} - \left(\rho\frac{U}{J}\right)_i\right\} - \theta b_1\left\{\left(\rho\frac{U}{J}\right)_i - \left(\rho\frac{U}{J}\right)_{i-1}\right\}}{a_1\Delta\zeta_1 - \theta b_1(\Delta\zeta_1 + \Delta\zeta_2)} \tag{10}$$

where

$a_1 = (\Delta\zeta_1 + \Delta\zeta_2)^2$
$b_1 = (\Delta\zeta_1)^2$
$\theta = 0$ first-order accurate
$= 1$ second-order accurate

Given the velocity potential ϕ information at all previous planes i, $i-1$, $i-2$,..., the problem is to compute ϕ at the current plane $i+1$. Equation (10) involves both the density and contravariant velocity at the $(i+1)$ plane, and both are functions of ϕ [Eq. (1)]. In order to write Eq. (10) in terms of ϕ will require only a local linearization procedure. This is done as follows:

$$(\rho U)_{i+1} \doteq (\rho U)_i + [(\rho U)_\phi]_i \Delta\phi + \ldots \tag{11}$$

where

$$(\rho U)_\phi = \rho_\phi U + \rho U_\phi \quad \text{and} \quad \Delta\phi = \phi_{i+1} - \phi_i$$

Substituting for ρ_ϕ and U_ϕ into Eq. (11), and grouping various term,

$$(\rho U)_{i+1} \doteq \rho_i\left[\left(a_{11} - \frac{U^2}{a^2}\right)_i \frac{\partial(\Delta\phi)}{\partial\zeta} + \left(a_{12} - \frac{UV}{a^2}\right)_i \frac{\partial(\Delta\phi)}{\partial\eta} + \left(a_{13} - \frac{UW}{a^2}\right)_i \frac{\partial(\Delta\phi)}{\partial\xi} + U_i\right] \tag{12}$$

The above locally linearized equation involves only $\Delta\phi$ as the unknown to be solved for. To maintain the conservative differencing, both $(\rho U)_{i+1}$ and $(\rho U)_i$ appearing in the first term of Eq. (10) will be linearized. That is, $(\rho U)_i$ will be linearized about $(i-1)$ plane values. The upwind differencing

of the ζ-derivative term as shown in Eq. (10) will produce a truncation term whose leading term is $\{1-(a^2a_{11}/U^2)\}U^2\phi_{\zeta\zeta\zeta}\Delta\zeta$. This will always represent a positive artificial viscosity as long as the marching condition dictated by the characteristic theory, Eq. (5), is satisfied.

C. Treatment of the Crossflow Term $(\rho V/J)_\eta$ in Eq. (1)

Similar to the treatment of the (ρU) term, the $(\rho V)_{i+1}$ will also be linearized as

$$(\rho V)_{i+1}=(\rho V)_i+[(\rho V)_\phi]_i\Delta\phi+\cdots$$
$$=\rho_i\left[\left(a_{21}-\frac{UV}{a^2}\right)_i\frac{\partial\Delta\phi}{\partial\zeta}+\left(a_{22}-\frac{V^2}{a^2}\right)_i\frac{\partial\Delta\phi}{\partial\eta}\right.$$
$$\left.+\left(a_{23}-\frac{VW}{a^2}\right)_i\frac{\partial\Delta\phi}{\partial\xi}+V_i\right] \tag{13}$$

The above linearized expression for $(\rho V)_{i+1}$ will be plugged inside the η-derivative term of Eq. (1). It involves only $\Delta\phi$ as the unknown variable. The finite-difference model for the $[\rho(V/J)]_\eta$ term will be dictated by the theory of characteristic signal propagation as described in Sec. II.A. When the eigenvalues of $A^{-1}B$ represent case 1 in Fig. 1 (one positive and one negative eigenvalue representing an elliptic type), then all of the terms in $[\rho(V/J)]_\eta$ will be central-differenced. For this case, $[a_{22}-(V^2/a^2)]$ is positive, and central differencing of the $[\rho(V/J)]_\eta$ term along with the backward differencing of the $[\rho(U/J)]_\zeta$ term as in Eq. (10) will preserve the diagonal dominance. For cases 2 and 3 of Fig. 1, the crossflow behaves like a hyperbolic type, and $[a_{22}-(V^2/a^2)]$ is negative. Then, central differencing of the terms in Eq. (13) is inappropriate, as it will destroy the diagonal dominance, and, in addition, will not provide the necessary artificial viscosity to avoid the formation of expansion shocks. Thus, when λ_1 and λ_2 are both positive or both negative (hyperbolic type), the terms in $[\rho(V/J)]_\eta$ should be upwind differenced depending on the direction of V. However, such an upwind differencing in the η direction will not give rise to a tridiagonal system and, in general, the overall system will be pentadiagonal in nature. In order to preserve the tridiagonal nature of the implicit scheme, rather than upwind differencing the ϕ derivatives, the density biasing concept[7,12] is implemented when the crossflow is hyperbolic.

The procedure is as follows:

$$\left(\rho\frac{V}{J}\right)_\eta\doteq\frac{\partial}{\partial\eta}\left\{\frac{\tilde\rho}{J}(a_{21}\phi_\zeta+a_{22}\phi_\eta+a_{23}\phi_\xi)\right\} \tag{14}$$

Here, the density ρ has been replaced by $\tilde\rho$ defined to be (referring to Fig. 2)

$$\tilde\rho_{i+1,j+\frac12,k}=(1-\nu_{i,j+\frac12,k})\rho^*_{j+\frac12,k}$$
$$+\tfrac12\nu_{i,j+\frac12,k}(\rho^*_{j+2m,k}+\rho^*_{j-1+2m,k}) \tag{15}$$

where $m=0$ when $V_{i,j+\frac12,k}>0$, $=+1$ when $V_{i,j+\frac12,k}<0$. The artificial viscosity coefficient $\nu_{i,j+\frac12,k}$ is computed as follows:

$$\nu_{i,j+\frac12,k}=\mu\left(1-\frac{a_{22}a^2}{V^2}\right)_{i,j+\frac12,k} \tag{16}$$

where a is the local speed of sound and

$$\mu=0 \text{ for } \left(a_{22}-\frac{V^2}{a^2}\right)_{i,j+\frac12,k}>0 \text{ (elliptic crossflow)}$$
$$=1 \text{ for } \left(a_{22}-\frac{V^2}{a^2}\right)_{i,j+\frac12,k}<0 \text{ (hyperbolic crossflow)}$$

Thus, the density biasing is switched off smoothly when the eigenvalues λ_1 and λ_2 exhibit an elliptic crossflow. All the ϕ-derivative terms are central differenced in Eq. (14). Treatment of the density as represented by Eqs. (15) and (16) would always produce a positive artificial viscosity when the crossflow is hyperbolic. The local total velocity is always assumed to be greater than the speed of sound, otherwise the marching procedure would fail.

In Eq. (15), the evaluation of ρ^* depends on whether the flow is conical or nonconical. For conical flows, all ρ^* quantities are evaluated at the ith plane. For nonconical flows, at each nonconical marching plane, initially ρ^* is set to be the value at the ith plane and then subsequently iterated to convergence by setting ρ^* to the previous iterated value of ρ at the current $i+1$ plane.

A similar density biasing procedure is implemented for the $[\rho(W/J)]_\xi$ term in Eq. (1).

Activating the density biasing based on the eigenvalue structure of $A^{-1}B$ and $A^{-1}C$ has proven to be very efficient in predicting sharp shock profiles. The same concept can also be employed for transonic applications.

D. Implicit Factorization Algorithm

Combining the various terms of Eq. (1) as represented by Eqs. (10, 14, and 15) together with the terms arising from $[\rho(W/J)]_\xi$ will result in a fully implicit model. This is solved using an approximate factorization implicit scheme. After some rearrangement of the terms, the factored implicit scheme becomes

$$\left[1+\frac{A_3}{\beta\Delta\zeta}\frac{\partial}{\partial\xi}+\frac{1}{\beta}\frac{\partial}{\partial\xi}\left(\frac{\tilde\rho}{J}\frac{a_{31}}{\Delta\zeta}\right)+\frac{1}{\beta}\frac{\partial}{\partial\xi}\frac{\tilde\rho a_{33}}{J}\frac{\partial}{\partial\xi}\right]$$
$$\times\left[1+\frac{A_2}{\beta\Delta\zeta}\frac{\partial}{\partial\eta}+\frac{1}{\beta}\frac{\partial}{\partial\eta}\left(\frac{\tilde\rho a_{21}}{J\Delta\zeta}\right)+\frac{1}{\beta}\frac{\partial}{\partial\eta}\frac{\tilde\rho a_{22}}{J}\frac{\partial}{\partial\eta}\right]\Delta\phi=R \tag{17}$$

which has the form

$$L_\xi L_\eta(\Delta\phi)=R \tag{18}$$

and is implemented as

$$L_\xi(\Delta\phi)^*=R,\quad L_\eta(\Delta\phi)=(\Delta\phi)^*,\quad \phi=\phi_i+\Delta\phi \tag{19}$$

The various quantities appearing in Eq. (17) are given by

$$\beta=\frac{A_1}{(\Delta\zeta)^2},\quad A_1=\frac{\rho_i}{J}\left(a_{11}-\frac{U^2}{a^2}\right)_i,\quad A_2=\frac{\rho_i}{J}\left(a_{12}-\frac{UV}{a^2}\right)_i,$$
$$A_3=\frac{\rho_i}{J}\left(a_{13}-\frac{UW}{a^2}\right)_i \tag{20}$$

and the right-hand-side term R consists of various known quantities. The algorithm Eq. (19) requires only scalar tridiagonal inversions.

III. Grid System

The transformation of the physical space (x,y,z) to a body-fitted computational space (ζ,η,ξ) is performed numerically by using the elliptic grid generation technique of Ref. 11. The body geometry at every marching plane is prescribed along with a suitable outer boundary where freestream conditions are imposed. Since the equation is cast in a general coordinate system, the marching plane (constant ζ) can either be a constant x plane or a spherical (constant r) plane as long as the marching criterion [Eq. (5)] is satisfied. Given the geometry shape and the prescribed outer boundary, the following set of elliptic equations are solved to generate the interior grid.

$$\xi_{yy}+\xi_{zz}=P(\xi,\eta),\qquad \eta_{yy}+\eta_{zz}=Q(\xi,\eta) \tag{21}$$

The forcing terms P and Q are properly chosen to achieve two main desirable features: 1) to cluster grid points to a bound-

ary, and 2) to force grid lines to intersect the boundary in a nearly orthogonal fashion.

Once the grid is generated, all the metric terms a_{ij} in Eq. (2) and the Jacobian J in Eq. (3) are computed by numerical differentiation. To subtract out any numerical truncation error in the freestream due to incomplete metric cancellation,[13] it is essential to add the term (especially for a high stretched nonorthogonal grid)

$$\frac{\partial}{\partial\zeta}\left(\frac{\rho_\infty U_\infty}{J}\right)+\frac{\partial}{\partial\eta}\left(\frac{\rho_\infty V_\infty}{J}\right)+\frac{\partial}{\partial\xi}\left(\frac{\rho_\infty W_\infty}{J}\right) \qquad (22)$$

to the right-hand side of the finite-differenced model of Eq. (1). To be consistent with the implicit operator, Eq. (18), the linearization procedures given by Eqs. (12) and (14) are also applied in evaluating Eq. (22).

IV. Results

A series of calculations were performed for conical and nonconical geometries at various Mach numbers ($M_\infty \sim 2$-6) and angles of attack ($\alpha \sim 0$-10 deg) to validate the full-potential characteristic switch methodology and assess the feasibility of using numerical grid solvers for complex configurations. The results from this study are compared with experimental data and Euler simulation.

The generality of the formulation allows one to choose any ζ as the marching direction, provided the condition given by Eq. (5) is satisfied. Thus, depending on the geometry definition and the flowfield character, one could choose either a constant x-plane marching or constant r-plane spherical marching.

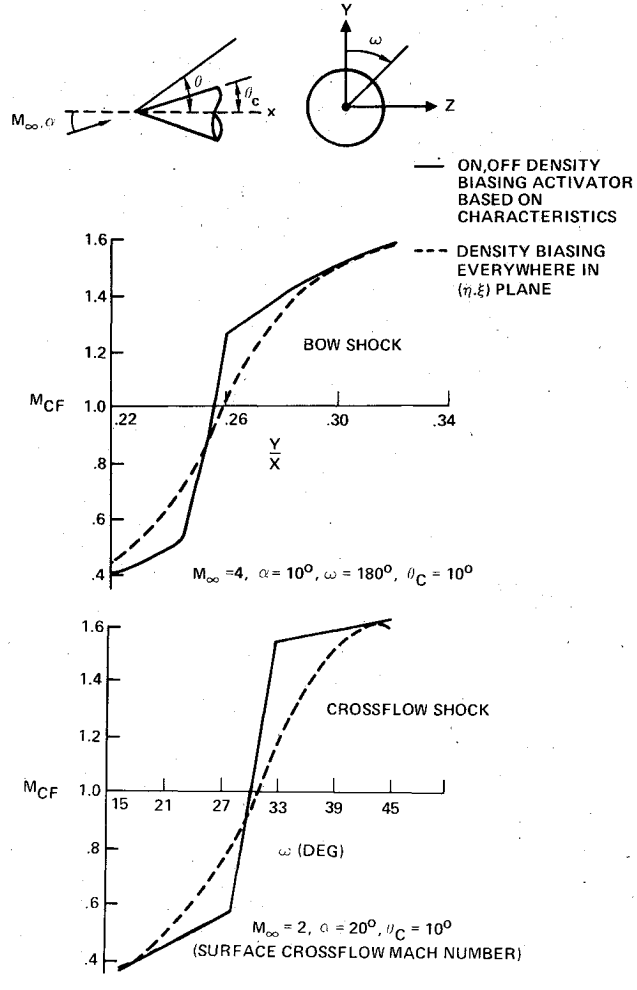

Fig. 3 Effect of density biasing activator on the crossflow Mach number distribution in the shock region.

The effect of on/off density biasing based on characteristic signals in the crossflow plane (η,ξ), described by Eq. (16), is demonstrated in terms of the crossflow Mach number (M_{CF}) distribution in the shock region in Fig. 3. When density

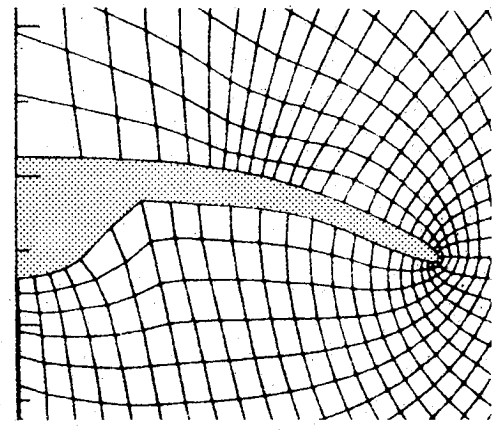

Fig. 4 Grid arrangement in the marching plane for a conically cambered wing-body combination.

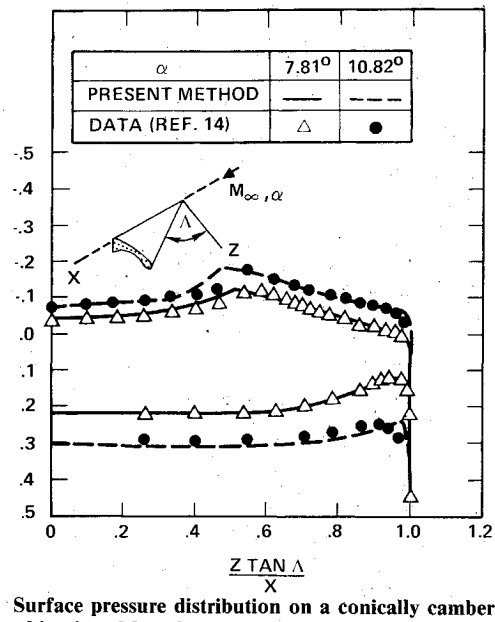

Fig. 5 Surface pressure distribution on a conically cambered wing-body combination, $M_\infty = 2$.

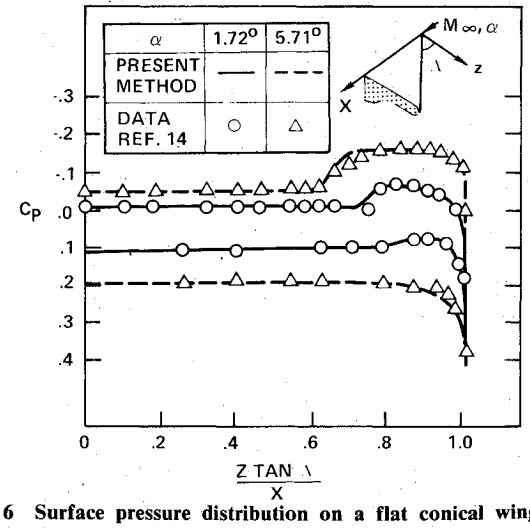

Fig. 6 Surface pressure distribution on a flat conical wing-body combination, $M_\infty = 2$.

biasing is applied everywhere,[7] including elliptic crossflow points, it introduces unnecessary artificial viscosity and tends to smear the discontinuities like shocks in the flowfield. This is seen by the dashed-line crossflow Mach number distribution across the bow shock and across the embedded shock on a cone surface in Fig. 3. When the density biasing is switched off at crossflow elliptic points, the shocks appear as a sharper discontinuity (usually within two mesh intervals), as shown by the solid line distribution in Fig. 3. All the calculations to be presented here were achieved using the second-order accurate implicit scheme [$\theta = 1$ in Eq. (10)], with on/off density biasing activator μ in Eq. (16).

Figure 4 shows the grid arrangement in the marching plane for a conically cambered wing-body combination. The elliptic grid solver with orthogonality constraints near the surface required 40-60 iterations to converge to within 10^{-8} error in the residual. Figure 5 shows the pressure distribution at $M_\infty = 2$ and angles of attack of 7.81 and 10.82 deg. The leading-edge sweep is moderate (57 deg), and spherical plane marching is implemented (instead of x-plane marching) to avoid low supersonic Mach number components along the x direction near the leading edge. The results are compared with experimental data given in Ref. 14. The comparison is excellent. The marching step size $\Delta\zeta$ is chosen by monitoring the eigenvalues and setting the Courant number to about 20. The numerical formulation, being a conservative form, predicts a stronger crossflow recompression on the leeward side than those seen in experiments. On a 20×49 (η, ξ) grid, the method requires about 1 min of CDC 7600 time. The conical flowfield is assumed to have converged when the change in root-mean-square density between two successive marching planes is reduced to less than 10^{-5}.

Figure 6 shows the surface pressure distribution on a flat conical wing-body (that is not designed to weaken the crossflow shock formation) at two different angles of attack (1.72 and 5.71 deg) and a Mach number of 2. The experimental data and the numerical prediction are in excellent agreement and clearly indicate the presence of an embedded crossflow shock.

Even though the full-potential theory is restricted by the isentropic assumption, one will be surprised to find that the

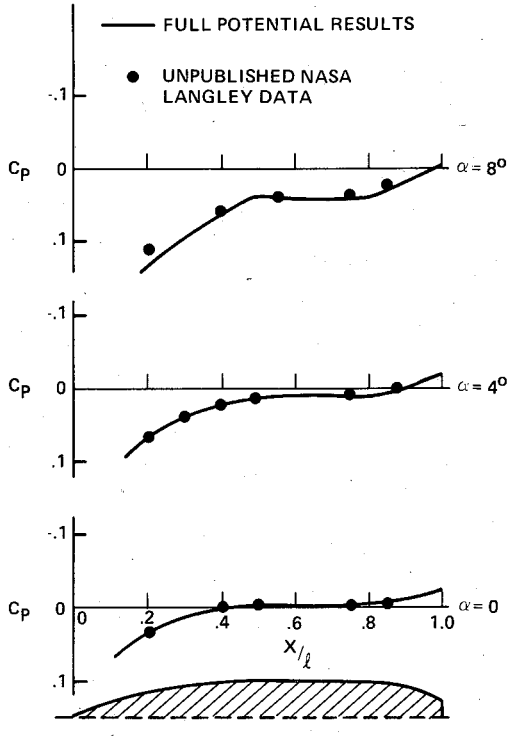

Fig. 7 Pressure distribution on Sears-Haack body at $M_\infty = 6$, windward plane of symmetry.

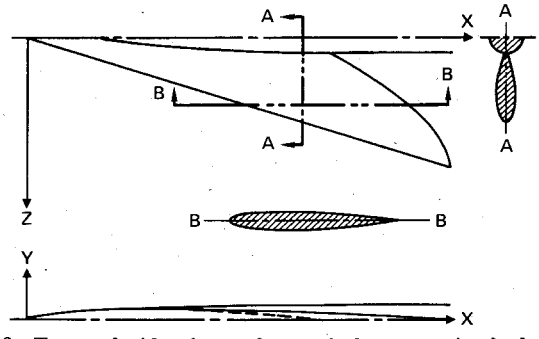

Fig. 8 Top and side views of a typical arrow wing-body configuration.

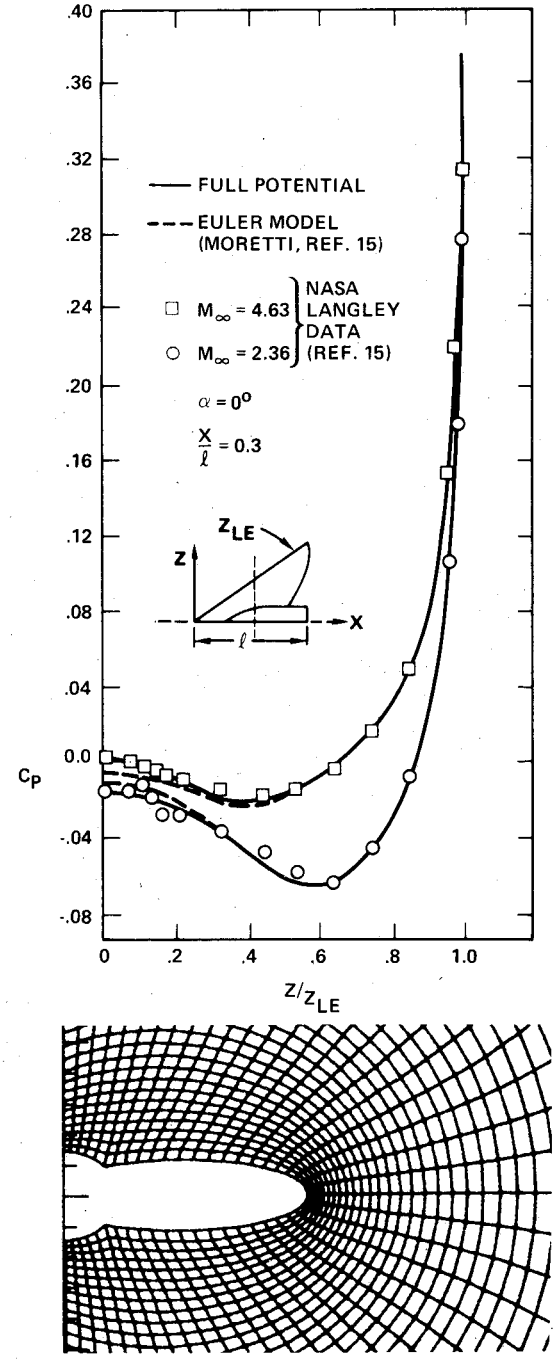

Fig. 9a Grid arrangement and surface pressure distribution for a symmetric arrow wing at $x/\ell = 0.3$.

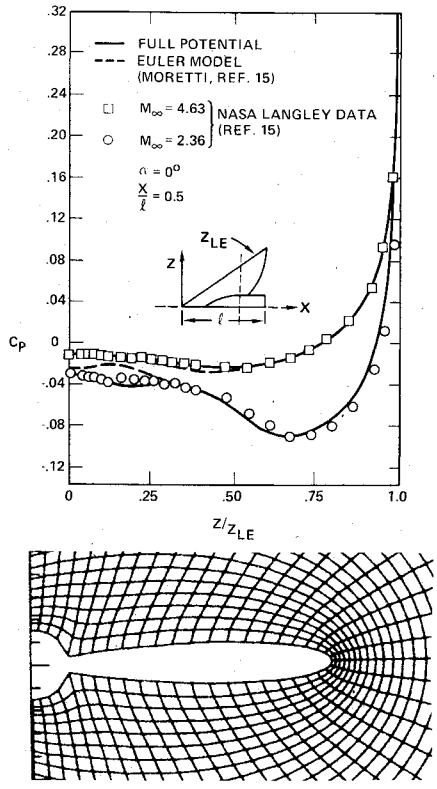

Fig. 9b Arrow wing pressure distribution at $x/\ell = 0.5$.

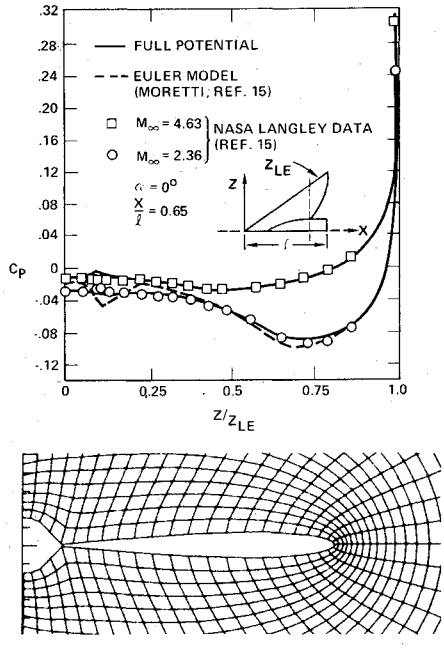

Fig. 9c Arrow wing pressure distribution at $x/\ell = 0.65$.

theory can be effectively utilized to predict even very high Mach number flows as long as $M\delta$ is less than or of the order of 1 ($M\delta \leq 1$). This is demonstrated in Fig. 7, which shows the results for a Sears-Haack body at $M_\infty = 6$ and different angles of attack (0, 4, and 8 deg). The numerical prediction is compared with unpublished NASA-Langley data, and the agreement is excellent. Constant x-plane marching is implemented for this configuration.

Figure 8 shows a schematic of a symmetric arrow wing-body configuration. The actual geometry shape is prescribed analytically as detailed in Ref. 15. A series of computer runs

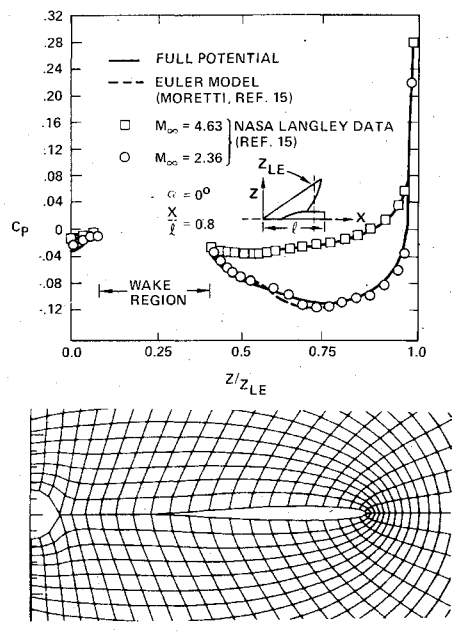

Fig. 9d Arrow wing pressure distribution at $x/\ell = 0.8$.

were made for this configuration at different Mach numbers and angles of attack and some results are presented here. First, an initial data plane near the nose region of the configuration is established by assuming a conical nose shape. The nonconical marching is then initiated. At each nonconical marching plane, the density is iterated to convergence [ρ^* in Eq. (15) usually takes 2-3 cycles to converge to 10^{-5} error tolerance] before proceeding to the next marching plane. The grid at each marching plane is generated using the elliptic grid solver. Figures 9a-d show a series of results at x/ℓ of 0.3, 0.5, 0.65, and 0.8, respectively. The full-potential results are compared with the experimental data and Euler simulation in Ref. 15. Figure 9a, which shows results for an x/ℓ of 0.3, clearly demonstrates the accuracy of the full-potential simulation. It is surprising to see that the present full-potential method compares with the experimental data even better than the Euler calculation, even at a high Mach number of 4.63. Similar excellent full-potential results are shown in Fig. 9b for an x/ℓ of 0.5 and compared with data from Ref. 15. The striking full-potential results are shown in Fig. 9c, where the unphysical oscillations experienced by the Euler simulation at $M_\infty = 2.36$ near the wing-body junction area are not seen in the present method, and comparison with experimental data is more dramatic. Figure 9d shows the pressure distribution at an x/ℓ of 0.8, where the wing is separated from the body. The wake is simulated by assuming a planar shape, and imposing pressure equality (in the present method, it will be density equality due to full-potential formulation) across the cut. Again, the full-potential results are in good agreement with the Euler solution and experimental data.

Figure 10 shows an angle-of-attack case, $M_\infty = 4.63$, $\alpha = 3$ deg for the same symmetric arrow wing-body configuration. The results are compared with the data of Ref. 15 at x/ℓ of 0.65, and the agreement is good even near the wing-body function region.

A typical arrow wing-body calculation using a 20×49 grid in the (η, ξ) plane and a marching step size Courant number of 3-5 [for a given Courant number, the predicted marching step size from Eq. (9) will decrease with decreasing freestream Mach number], required approximately 2-3 min of CPU time for the entire calculation. This includes the numerical grid generation at each plane and the conical initial data plane and represents an enormous savings in computer execution cost over other nonlinear methods, especially Euler solvers.

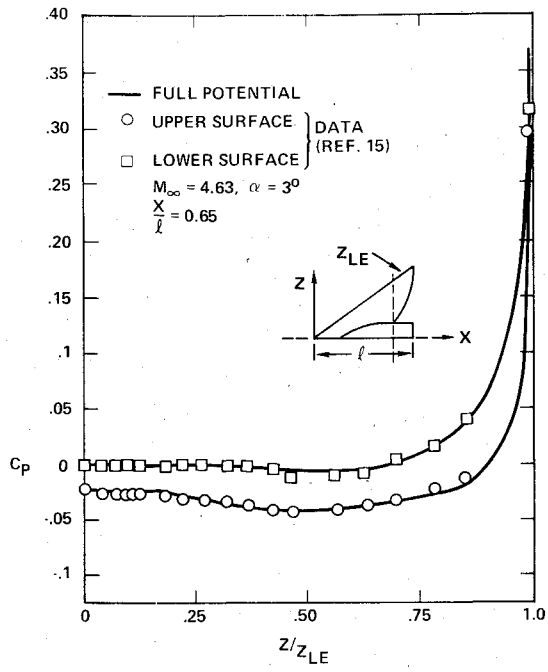

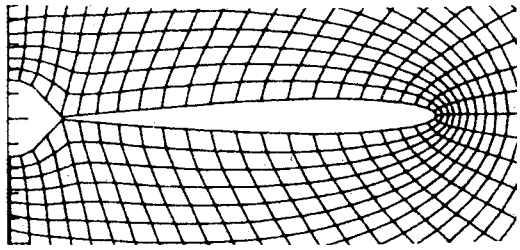

Fig. 10 Angle-of-attack solution for the arrow wing at $x/\ell = 0.65$.

V. Conclusions

A nonlinear full-potential aerodynamic prediction capability based on a sound mathematical theory of characteristic signal propagation has been developed. The method uses a general body-fitted coordinate system and numerical mapping techniques. The on/off density biasing activator in the crossflow plane has proved to be very effective in capturing sharp shock profiles. Results for conical and nonconical flows at various Mach numbers and angles of attack are shown to be in excellent agreement with experimental data and Euler results. The enormous savings in computational cost exhibited by the present approach makes it a very promising substitute for the less accurate linearized panel methods and expensive Euler solvers, for use as a preliminary design tool. Future work will involve automatic grid generation for wing-body-nacelle-canard configurations and better wake treatment.

Appendix—Derivation of the Marching Condition [Eq. (5)] for a Cartesian System

The Cartesian system analog of Eq. (4) is given by

$$Af_x + Bf_y + Cf_z = 0 \tag{A1}$$

where

$$A = \begin{bmatrix} (\rho u)_u & (\rho u)_v & (\rho u)_w \\ 0 & 1 & 0 \\ 0 & 0 & 1 \end{bmatrix}$$

$$B = \begin{bmatrix} (\rho v)_u & (\rho v)_v & (\rho v)_w \\ -1 & 0 & 0 \\ 0 & 0 & 0 \end{bmatrix}$$

$$C = \begin{bmatrix} (\rho w)_u & (\rho w)_v & (\rho w)_w \\ 0 & 0 & 0 \\ -1 & 0 & 0 \end{bmatrix}$$

$$f = \begin{bmatrix} u \\ v \\ w \end{bmatrix}$$

Equation (A1) is hyperbolic with respect to the x direction if 1) A^{-1} exist, and 2) $A^{-1}(\alpha B + \beta C)$ must have real eigenvalues for all α and β satisfying $\alpha^2 + \beta^2 = 1$.

Since A^{-1} is assumed to exist, the eigenvalues of $A^{-1}(\alpha B + \beta C)$ can be obtained by setting the following determinant to zero.

$$|\alpha B + \beta C - \lambda A| = 0 \tag{A2}$$

Substituting for A, B, and C from Eq. (A1) into Eq. (A2), the roots of the equation are obtained.

$$\lambda_{1,2} = \left[-\frac{u}{a^2}(v\alpha + w\beta) \pm \sqrt{\frac{u^2}{a^4}(v\alpha + w\beta)^2 - \left(1 - \frac{u^2}{a^2}\right)\left\{1 - \frac{(v\alpha + w\beta)^2}{a^2}\right\}} \right] \Big/ \left(1 - \frac{u^2}{a^2}\right) \tag{A3}$$

Equation (A3) will have real values as long as the square root term is real. This implies the quantity inside the square root must be positive. Simplifying the quantity inside the square root, the condition becomes

$$\frac{u^2 + (v\alpha + w\beta)^2}{a^2} - 1 > 0 \tag{A4}$$

Let

$$\left.\begin{aligned} \alpha &= \cos\theta \\ \beta &= \sin\theta \end{aligned}\right\} \Rightarrow \alpha^2 + \beta^2 = 1$$

$$v = \bar{q}\cos\bar{\theta}, \qquad w = \bar{q}\sin\bar{\theta}$$

where

$$\bar{q} = \sqrt{v^2 + w^2}, \qquad \tan\bar{\theta} = w/v$$

Substituting these into Eq. (A4) and simplifying results in

$$\frac{u^2 + \bar{q}^2\cos^2(\bar{\theta} - \theta)}{a^2} - 1 > 0 \tag{A5}$$

Since this condition must hold for all combinations of θ and $\bar{\theta}$, Eq. (A5) implies (for $\bar{\theta} - \theta = \pi/2$)

$$\boxed{\frac{u^2}{a^2} - 1 > 0} \quad \text{for } x \text{ to be the marching direction} \tag{A6}$$

Equation (A6) is a special case of Eq. (5) in Sec. II.

Acknowledgment

This work was supported in full by NASA-Langley Research Center under Contract NAS1-15820.

References

[1]Marconi, F., Salas, M., and Yeager, L., "Development of a Computer Code for Calculating the Steady Super/Hypersonic Inviscid Flow Around Real Configurations, Vol. I—Computational Techniques," NASA CR 2675, April 1976.

[2]Kutler, P., "Computation of Three-Dimensional, Inviscid Supersonic Flows," in *Lecture Notes in Physics 41*, Springer-Verlag, New York, 1975, pp. 287-374.

[3]Siclari, M. J., "Investigation of Cross Flow Shocks on Delta Wings in Supersonic Flow," *AIAA Journal*, Vol. 18, Jan. 1980, p. 85.

[4]Grossman, B., "Numerical Procedure for the Computation of Irrotational Conical Flows," *AIAA Journal*, Vol. 17, Aug. 1979, pp. 828-837.

[5]Grossman, B. and Siclari, M. J., "The Nonlinear Supersonic Potential Flow over Delta Wings," AIAA Paper 80-0269, Pasadena, Calif., Jan. 1980.

[6]Siclari, M. J., "Computation of Nonlinear Supersonic Potential Flow over Three-Dimensional Surfaces," AIAA Paper 82-0167, presented at the AIAA 20th Aerospace Sciences Meeting, Orlando, Fla., Jan. 1982.

[7]Shankar, V., "A Conservative Full Potential, Implicit, Marching Scheme for Supersonic Flows," *AIAA Journal*, Vol. 20, Nov. 1982, pp. 1508-1514.

[8]Carmichael, R. L. and Erickson, L. L., "Pan Air—A Higher Order Panel Method for Predicting Subsonic or Supersonic Linear Potential Flows about Arbitrary Configurations," AIAA Paper 81-1255.

[9]Jameson, A., "Transonic Potential Flow Calculations using Conservation Form," *AIAA Second Computational Fluid Dynamics Conference Proceedings*, 1975, pp. 148-155.

[10]Lax, P. D., "Weak Solutions of Nonlinear Hyperbolic Equations and Their Numerical Computation," *Communications on Pure and Applied Mathematics*, Vol. 7, No. 1, Jan. 1954, pp. 159-193.

[11]Steger, J. L. and Sorenson, R. L., "Automatic Mesh-Point Clustering Near a Boundary in Grid Generation with Elliptic Partial Differential Equations," *Journal of Computational Physics*, Vol. 33, No. 3, Dec. 1979, p. 405.

[12]Holst, T. L., "Fast, Conservative Algorithm for Solving the Transonic Full Potential Equation," *AIAA Journal*, Vol. 18, Dec. 1980, pp. 1431-1439.

[13]Steger, J. L. and Caradona, F. X., "A Conservative Implicit Finite Difference Algorithm for the Unsteady Transonic Full Potential Equation," FSI Rept. 79-04, Dec. 1979.

[14]Miller, D. S., Landrum, E. J., Townsend, J. C., and Mason, W. H., "Pressure and Force Data for a Flat Wing and a Warped Conical Wing Having a Shockless Recompression at Mach 1.62," NASA TP 1759, April 1981.

[15]Townsend, J. C., "Pressure Data for Four Analytically Defined Arrow Wings in Supersonic Flow," NASA TM 81835, Sept. 1980.